Supplementary Information

Sandwich-like Heterometallic Fe_7Sn_6 Oxo Cluster Constructed by Tessellation of Anderson-like {Fe_7} Wheel for Near-infrared Photothermal Conversion

Xiu-Juan Tian[‡a], Qian Lu[‡a], Shi-Li Li*[a] and Xian-Ming Zhang*[a,b]

[a] Key Laboratory of Magnetic Molecules and Magnetic Information Materials (Ministry of Education), College of Chemistry & Material Science, Shanxi Normal University, Taiyuan 030031, P. R. China.

[b] College of Chemistry & Chemical Engineering, Taiyuan University of Technology, Taiyuan, 030024, P. R. China.

‡ These authors contributed equally to this work and should be considered co-first authors.

E-mails: zhangxm@dns.sxnu.edu.cn; lisl@sxnu.edu.cn.

Materials and Instruments.

All of the chemicals were used without further purification after being purchased from suppliers. Diacetoxy(hydroxy)iron was purchased from Macklin, butyltin hydroxide oxide and 2,6-pyridinedicarboxylic acid were supplied by Aladdin, while acetonitrile and isopropanol were bought from Tianjin Kemiou Chemical Reagent Co., Ltd. Infrared spectrum (IR) was obtained in the range of 4000–400 cm^{-1} on an FTIR-650 spectrometer using KBr pellets method. Powder XRD patterns were collected on a MiniFlex600 benchtop powder diffractometer with Cu K_α radiation (λ = 1.54056 Å) at room temperature. Solid-state UV−vis spectra were recorded on a TU-1901 double-beam UV−vis spectrophotometer using $BaSO_4$ with 100% reflectivity as a standard. Elemental content analyses of Fe, Sn and N were measured by inductively coupled plasma emission spectrometry (Agilent 5110 ICP-OES) and oxygen and nitrogen analyzer (ELEMENTRAC ONH-p 2), respectively. Thermogravimetric analysis (TGA) was conducted by a Netsch STA449F5 thermal analyzer in a flowing nitrogen gas atmosphere with a rate of 10 °C min^{-1} from room temperature to 800 °C. The light source for photothermal conversion tests was provided by an MDL-III-808-2W 808 nm laser, and the real-time temperature was collected by a KSD01A0R paperless recorder. The light source for solar-driven water evaporation experiments was a CEL-S500-T5 Xenon lamp with optical filter (AM 1.5), while the temperature during experiments were recorded using an FPI-Pi33L-L25 infrared camera.

Synthesis of $[Fe_7(BuSn)_6(O)(OH)_{11}(\mu_4\text{-}O)_6(L)_6][Fe(L)_2]_2\cdot 5H_2O\cdot 2CH_3CN\cdot 2i$PrOH.

150 mg diacetoxy(hydroxy)iron, 167 mg 2,6-pyridinarboxylic acid, 209 mg butyltin hydroxide oxide, 6 mL acetonitrile, 1 mL water and 1 mL isopropanol were mixed in the Teflon-lined autoclave (15 mL), and stirred for about 30 min. The resulting orange mixture was heated at 100 °C for 4 days. After cooling to room temperature, the resulting products were filtered and washed thoroughly with acetonitrile, then orange rhombohedral crystals suitable for X-ray analysis were obtained. Yield: 0.056 g (44.21% yield based on Fe). Elemental analysis (%) calcd (found) for

$Fe_9Sn_6C_{104}H_{127}N_{12}O_{65}$: Fe, 13.23 (10.11); Sn 18.74 (16.54), N 4.42 (3.65). IR (KBr, pellet, cm^{-1}): 2956 (w), 1704 (s),1428 (w), 1336 (s), 1168 (m), 1074 (m), 918 (w), 739 (m), 578 (m).

Single-crystal X-ray diffraction.

The crystallographic data of **Fe_7Sn_6** were collected on a Rigaku XtaLAB PRO 007HF (Cu) single crystal diffractometer with CuK_α radiation source (λ = 1.54178 Å) at 150 K. The structure was solved by direct methods in Olex2 software with the ShelXT program and refined with Full matrix least-squares methods based on F^2 using ShelXL program.[1,2] Non-hydrogen atoms were refined anisotropically, and hydrogen atoms were added theoretically and refined with fixed thermal factors. Some disordered solvent molecules in **Fe_7Sn_6** were removed using the SQUEEZE routine of PLATON[3] and the numbers of these solvent molecules are determined by elemental analysis and TGA. CCDC 2342707 contains the supplementary crystallographic data for this paper and the selected crystallographic data are summarized in Table S1.

Table S1. Crystallographic Information of **Fe_7Sn_6**.

Compound	**Fe_7Sn_6**
Formula	$Fe_9Sn_6C_{104}H_{127}N_{12}O_{65}$
Fw	3800.0281
Crystal system	Monoclinic
space group	*P*21/*c*
T (K)	149.99(10)
Wavelength [Å]	1.54178
a [Å]	16.55940(10)
b [Å]	22.4100(2)
c [Å]	23.2623(2)
α [°]	90

β [°]	129.2710(10)
γ [°]	90
V [Å^3]	6682.97(12)
Z	2
ρ_{calcd} [g·cm^{-3}]	1.761
F (000)	3494
μ [mm^{-1}]	17.121
Reflections collected	166234
Independent reflections	11769
Completeness	99.6%
GOF (F^2)	1.057
R_1/wR_2 [$I > 2\sigma(I)$]	0.0769/0.2373
R_1/wR_2[a] (all data)	0.0800/0.2405

[a] $R_1 = \Sigma||F_o|-|F_c||/\Sigma|F_o|$, $wR_2 = [\Sigma w(F_o^2 - F_c^2)^2/\Sigma w(F_o^2)]^{1/2}$.

Table S2. Selected bond lengths (Å) for **Fe$_7$Sn$_6$**.

Bond	Length (Å)	Bond	Length (Å)
Sn(1)-O(00A)	2.052(5)	Fe(2)-O(00A)	2.003(5)
Sn(1)-O(00I)	2.077(5)	Fe(2)-O(00B)#1	2.009(5)
Sn(1)-O(00L)	2.065(6)	Fe(2)-O(00B)	2.009(5)
Sn(1)-O(00M)	2.235(5)	Fe(2)-O(00E)	1.996(5)
Sn(1)-O(00N)	2.209(5)	Fe(2)-O(00E)#1	1.996(5)
Sn(1)-C(01W)	2.106(9)	Fe(3)-O(00A)	2.145(5)
Sn(2)-O(00E)	2.043(5)	Fe(3)-O(00D)	1.920(5)
Sn(2)-O(00F)#1	2.216(5)	Fe(3)-O(00E)#1	2.131(5)
Sn(2)-O(00G)#1	2.199(6)	Fe(3)-O(00G)	2.178(6)
Sn(2)-O(00I)	2.041(6)	Fe(3)-O(00H)	1.938(5)
Sn(2)-O(00J)	2.052(5)	Fe(3)-O(00N)	2.188(6)
Sn(2)-C(01E)	2.079(11)	Fe(3)-N(2)	2.138(6)

Sn(3)-O(00B)	2.028(5)	Fe(4)-O(009)	1.953(5)
Sn(3)-O(00C)#1	2.222(6)	Fe(4)-O(00B)	2.138(5)
Sn(3)-O(00J)	2.049(6)	Fe(4)-O(00D)	1.940(5)
Sn(3)-O(00K)	2.202(5)	Fe(4)-O(00E)#1	2.120(5)
Sn(3)-O(00L)	2.073(6)	Fe(4)-O(00F)	2.179(5)
Sn(3)-C(01N)	2.076(13)	Fe(4)-O(00K)	2.173(6)
Fe(1)-O(009)#1	1.940(5)	Fe(4)-N(3)	2.149(6)
Fe(1)-O(00A)	2.133(5)	Fe(5)-O(00T)	2.075(8)
Fe(1)-O(00B)#1	2.135(5)	Fe(5)-O(00X)	2.039(11)
Fe(1)-O(00C)	2.188(6)	Fe(5)-O(012)	1.968(9)
Fe(1)-O(00H)	1.937(5)	Fe(5)-O(01A)	2.016(9)
Fe(1)-O(00M)	2.173(6)	Fe(5)-N(4)	2.067(9)
Fe(1)-N(1)	2.154(6)	Fe(5)-1N(5)	1.964(7)
Fe(2)-O(00A)#1	2.003(5)		

Symmetry transformations used to generate equivalent atoms: #1 -x+2,-y+1,-z+1

Table S3. Optical band gaps of some reported tin-oxo clusters.

Compounds	Bandgaps (eV)	Reference
γ-[(n-BuSn)$_{14}$(OCH$_3$)$_{10}$(OH)$_3$O$_9$(NaO$_4$)(HBO$_3$)$_2$]	4.46	[4]
γ-[(n-BuSn)$_{14}$(OCH$_3$)$_{10}$(OH)$_3$O$_9$(NaO$_4$)(PhO$_2$)$_2$]	4.39	
[(^{n}BuSn)$_{13}$(H$_2$O)(OH)$_{14}$O$_{10}$(INA)$_2$](INA)$_3$·5H$_2$O·2CH$_3$CH$_2$OH	3.90	[5]
[(^{n}BuSn)$_{13}$(H$_2$O)(OH)$_{14}$O$_{10}$(TZ1AC)$_2$](TZ1AC)$_3$·3H$_2$O	4.52	
NaH[(^{n}BuSn)$_3$(PDC)$_3$(OCH$_3$)(OH)$_3$]$_2$·6CH$_3$OH	3.76	[6]
(^{n}BuSn)$_6$O$_2$(PP)$_4$(OCH$_3$)$_6$	4.46	
[(^{n}BuSn)$_{12}$(OH)$_{18}$O$_4$(BPA)$_2$(H$_2$BPA)$_4$]·6H$_2$O	5.26	
[(^{n}BuSn)$_{22}$Sn$_4$(OH)$_{26}$O$_{22}$(IANO)$_6$][(^{n}BuSn)$_2$(OH)$_2$(IANO)Cl$_4$]$_2$·4Cl·6 CH$_3$OH·10H$_2$O	3.69	
[(^{n}BuSn)$_{34}$Na$_2$(OH)$_{14}$O$_{40}$(PA)$_8$]·2(PA)·8H$_2$O	3.99	
[Na$_6$(^{n}BuSn)$_{14}$(OH)$_8$O$_4$(APA)$_{16}$]·12H$_2$O	3.86	[7]

$[(^{n}BuSn)_2(TEOA)_2(3\text{-}TPC)_2]$	4.43	
$[(^{n}BuSn)_2(TEOA)_2(BC)_2]$	4.30	[8]
$[(^{n}BuSn)_2(TEOA)_2(4HB_5CA)_2]$	3.89	
$\{Na_4(H_2O)_2[(^{n}BuSn)_6(OH)_{10}(C_2O_4)_4]_2\}\cdot 2CH_3OH\cdot 13H_2O$	4.19	[9]
$[Na_3(^{n}BuSn)_9(OH)_6(L_1)_6(L_2)_3]$ $5(C_2H_5OH)$	5.09	[10]
$(^{n}BuSn)_5(\mu_3\text{–}O)_2(EG)_4(tbba)_3$	3.82	[11]
$(^{n}BuSn)_5(\mu_3\text{–}O)_2(EG)_4(4\text{-}BA)_3$	4.18	
$[(BuSn)_{12}Sn_6(\mu_3\text{–}O)_{20}(ba)_{12}(PhPO_3)_4]$	4.17	
$[(BuSn)_{12}Sn_6(\mu_3\text{–}O)_{20}(pmba)_{12}(PhPO_3)_4]\cdot 2CH_3CN\cdot 2H_2O$	3.94	[12]
$[(BuSn)_{12}Sn_6(\mu_3\text{–}O)_{20}(ptba)_{12}(PhPO_3)_4]\cdot 2CH_3CN\cdot 2i\text{PrOH}\cdot 2H_2O$	4.19	
$[Fe_7(BuSn)_6(O)(OH)_{11}(\mu_4\text{-}O)_6(L)_6][Fe(L)_2]_2\cdot 5H_2O\cdot 2CH_3CN\cdot 2i\text{PrOH}$	2.72	Our work

Table S4 Selected Metal–O/N bond lengths of **Fe_7Sn_6**.

Compounds	**Fe–N**	**Fe–O**	**Sn–O**
Bond length range (Å)	1.951–2.150	1.919–2.187	2.028–2.230
Average bond length (Å)	2.0882	2.0655	2.1167

Bond valence sum calculation

The oxidation states of Fe in **Fe_7Sn_6** were estimated by bond valence sum (BVS) calculation (equation a and b), giving the Fe charge states range of 2.57–2.71 (using Fe^{2+} parameters, not self-consistent) and 3.04–3.17 (using Fe^{3+} parameters). These results were summarized in Table S6 and confirms that all Fe atoms in the cluster are in the charge state of +3.

$$S = \exp\left(\frac{R_0 - R}{b}\right) \quad \text{(a)}$$

$$S = \text{sum}\ (S_j) \quad \text{(b)}$$

Where S is a function of bond length, R is the length of the bond, R_0 and b are list in Table S5, which were obtained from the website

https://www.iucr.org/resources/data/data-sets/bond-valence-parameters.

Table S5 Parameters of Fe-related bonds in **Fe_7Sn_6**.

	R_0/b (Å)	**O (–2)**	**N (–3)**
	Fe (+2)	1.700/0.37	1.769/0.37
	Fe (+3)	1.765/0.37	1.815/0.37

Table S6 Details of the BVS calculation for Fe in **Fe_7Sn_6**.

Atom	**Bond**	**Bond length (Å)**	**Valence (+2)**	**Valence (+3)**
Fe(1)	Fe(1)-O(009)#1	1.940(5)	0.5228	0.6232
	Fe(1)-O(00A)	2.133(5)	0.3103	0.3699
	Fe(1)-O(00B)#1	2.135(5)	0.3086	0.3679
	Fe(1)-O(00C)	2.188(6)	0.2674	0.3188
	Fe(1)-O(00H)	1.937(5)	0.5270	0.6282
	Fe(1)-O(00M)	2.173(6)	0.2785	0.3320
	Fe(1)-N(1)	2.154(6)	0.3533	0.4000
Sum	–	–	2.5679	3.0400
Fe(2)	Fe(2)-O(00A)#1	2.003(5)	0.4409	0.5256
	Fe(2)-O(00A)	2.003(5)	0.4409	0.5256
	Fe(2)-O(00B)#1	2.009(5)	0.4338	0.5171
	Fe(2)-O(00B)	2.009(5)	0.4338	0.5171
	Fe(2)-O(00E)	1.996(5)	0.4493	0.5356
	Fe(2)-O(00E)#1	1.996(5)	0.4493	0.5356
Sum	–	–	2.6480	3.1566
Fe(3)	Fe(3)-O(00A)	2.145(5)	0.3004	0.3581
	Fe(3)-O(00D)	1.920(5)	0.5518	0.6578
	Fe(3)-O(00E)#1	2.131(5)	0.3120	0.3719
	Fe(3)-O(00G)	2.178(6)	0.2748	0.3275
	Fe(3)-O(00H)	1.938(5)	0.5256	0.6265

	Fe(3)-O(00N)	2.188(6)	0.2674	0.3188
	Fe(3)-N(2)	2.138(6)	0.3689	0.4177
Sum	–	–	2.6009	3.0783
Fe(4)	Fe(4)-O(009)	1.953(5)	0.5047	0.6016
	Fe(4)-O(00B)	2.138(5)	0.3061	0.3649
	Fe(4)-O(00D)	1.940(5)	0.5228	0.6232
	Fe(4)-O(00E)#1	2.120(5)	0.3214	0.3831
	Fe(4)-O(00F)	2.179(5)	0.2740	0.3266
	Fe(4)-O(00K)	2.173(6)	0.2785	0.3320
	Fe(4)-N(3)	2.149(6)	0.3581	0.4055
Sum	–	–	2.5656	3.0369
Fe(5)	Fe(5)-O(00T)	2.075(8)	0.3629	0.4326
	Fe(5)-O(00X)	2.039(11)	0.4000	0.4769
	Fe(5)-O(012)	1.968(9)	0.4847	0.5777
	Fe(5)-O(01A)	2.016(9)	0.4257	0.5074
	Fe(5)-N(4)	2.067(9)	0.4469	0.5061
	Fe(5)-1N(5)	1.964(7)	0.5904	0.6685
Sum	–	–	2.7106	3.1692

Photothermal Conversion Efficiency Measurement.

Referring the method described in literatures,[13–15] we further optimised the test platform to determine the photothermal conversion (PTC) effect of **Fe_7Sn_6** more accurately. (Figure S1). Specifically, 13 mg **Fe_7Sn_6** powder was encapsulated in two custom quartz slides to manufacture a small photothermal device. The quartz slides in the device had a total mass of 0.655 g and all had dimensions of 1.2 × 1.2 × 0.1 cm^3, with one having a circular groove of 0.8 cm in diameter and 0.03 cm in depth. Under the irradiation of an 808 nm-laser, the real-time temperature on device surface were collected by a paperless recorder in series with a thermal sensor. To obtain accurate absorption values of the encapsulated sample, UV–vis absorption spectra of the

device were measured directly. The photothermal conversion efficiency (η) was precisely calculated according to the following procedure.

The balance equation for the total energy of the test system is:

$$\sum_i m_i C_{p,i} \frac{dT}{dt} = Q_s - Q_{loss} \quad (1\text{-}1)$$

$$\sum_i m_i C_{p,i} = m_s \cdot C_s + m_q \cdot C_q \quad (1\text{-}2)$$

Wherein, m_i / $C_{p,i}$: the relevant mass and specific heat capacity in the test system.
m_s / m_q : the mass of the sample (0.013 g) / quartz groove (0.655 g).
C_s / C_q : the specific heat capacity of the sample (0.682 $J \cdot g^{-1}$ $°C^{-1}$) / quartz (0.8 $J\ g^{-1}$ $°C^{-1}$). The specific heat capacity of **Fe_7Sn_6** was obtained by DSC test, and then the average value was taken in the range of 20–55 ℃ to calculate the required C_s.
Q_s : photothermal energy obtained by the sample during laser irradiation.
Q_{loss} : heat energy lost to the environment.

When the temperature reaches its maximum, the system is in equilibrium:

$$Q_s - Q_{loss} = hs\Delta T_{max} \quad (1\text{-}3)$$

Where h is the heat transfer coefficient, S is the surface area of the system, and ΔT_{max} is the maximum temperature change. Therefore, the photothermal conversion efficiency η can be calculated by the following equation:

$$\eta = \frac{hs\Delta T_{max}}{I(1 - 10^{-A_{808}})} \quad (1\text{-}4)$$

In which I is the laser power (1.4 W cm^{-2}) and A_{808} is the absorbance of the sample at 808 nm (0.076).

To obtain the value of hS in equation (1-4), a dimensionless drive temperature θ is introduced:

$$\theta = \frac{T - T_{surr}}{T_{max} - T_{surr}} \quad (1\text{-}5)$$

Here, T and T_{max} (54.3 °C) are the real-time temperature and maximum temperature

of the device; T_{surr} (21.8 °C) is the initial temperature.

The time constant τ_s of the test system is obtained from equation (1-1):

$$\tau_s = \frac{\sum_i m_i C_{p,i}}{hs} \tag{1-6}$$

Then:

$$\frac{d\theta}{dt} = \frac{1}{\tau_s} \cdot \frac{Q_s}{hs\Delta T_{max}} - \frac{\theta}{\tau_s} \tag{1-7}$$

When the laser is off, $Q_s = 0$, i.e.:

$$\frac{d\theta}{dt} = -\frac{\theta}{\tau_s}$$

Therefore:

$$t = -\tau_s ln\theta \tag{1-8}$$

From the slope of the time-lnθ curve after cooling, τ_s (83.31±0.31) was obtained and then hS was calculated using equation (1-6). Substitution of hS into equation (1-4) results in a photothermal conversion efficiency of 92.44±0.44% for **Fe_7Sn_6**.

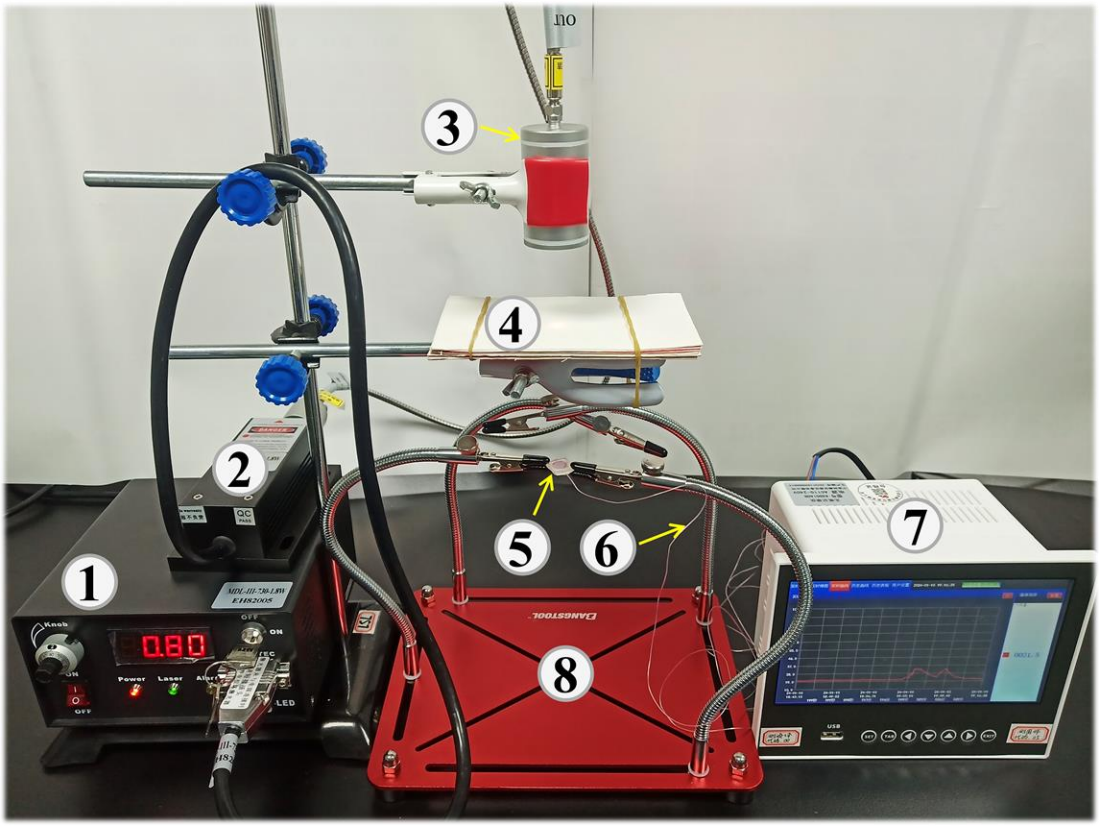

Figure S1. Schematic of a self-assembling device for photothermal conversion tests.

Wherein, ①, ② and ③ 808nm laser transmitter with tunable output power; ④ Homemade whiteboards for laser masking; ⑤ Micro-device encapsulated with sample powder; ⑥ Surface mounted thermocouple; ⑦ Paperless recorder; ⑧ Multi-purpose clamping table.

Solar-driven Water Evaporation Measurement.

Based on the principle of interfacial evaporation, we built a solar-driven water evaporation device. Specifically, 35 mg of **Fe_7Sn_6** was loaded onto a circular cellulose paper with a diameter of 2.1 cm and placed on the water surface to fabricate a simple solar-driven water evaporator for interfacial heating and water evaporation (Figure 4a). A Xenon lamp with optical filter (AM 1.5) was used to simulate 1-sun (1 Kw m^{-2}) and the temperature change of **Fe_7Sn_6**-cellulose paper was recorded over a period of 15 min exposure to simulated 1-sun intensity. As shown in Figure 4b, the temperature of **Fe_7Sn_6**-cellulose paper can reach 45 °C, while the blank cellulose paper is only 29 °C under the same conditions.

The solar-driven water evaporation experiment was performed by floating **Fe_7Sn_6**-cellulose paper floated on water surface of a beaker and exposing it under simulated 1-sun intensity for 1 h, while the surface temperature change of the evaporator and the water mass loss were recorded by infrared thermography and electronic balance, respectively. According to the water mass loss versus time dependence curve (Figure 4d), the water evaporation rate of **Fe_7Sn_6**-cellulose paper was higher than that of blank cellulose paper and pure water, which were 0.71 kg m^{-2} h^{-1}, 0.61 kg·m^{-2} h^{-1} and 0.55 kg·m^{-2} h^{-1}, respectively. The solar-driven water evaporation efficiency of **Fe_7Sn_6**-cellulose paper is 34.94% and the specific calculation procedure is as follows: [16–18]

$$\eta = \frac{\dot{m} h_{LV}}{C_{opt} P_o} \qquad (2\text{-}1)$$

Where $\dot{m}$ is the water evaporation rate of the evaporator under solar illumination, it

can be calculated using formula of $\dot{m} = m_{light} - m_{blank}$, in which, m_{light} refers to the water evaporation rate of evaporator irradiated by simulated sunlight in 1 h, while m_{blank} represents the water evaporation rate of the evaporator in 1 h under environmental conditions. P_o is the solar radiation value of 1 Kw m^{-2}; and C_{opt} is denoted as the optical concentration (It is a constant of 1 in this work). h_{LV} indicates the sensible heat and latent heat of total liquid-vapor phase-change, it is caculated by formula 2-2.

$$h_{LV} = Q + \Delta h_{vap} \quad (2\text{-}2)$$

Where Q is the energy used to transform the system from its initial temperature T_0 to the final temperature T, Δh_{vap} refers to the latent heat of vaporization of water and it can be obtained from formula 2-3.

$$Q = C_{liquid} \times (T - T_0) \quad (2\text{-}3)$$

$$\Delta h_{vap} = Q_1 + \Delta h_{100} + Q_2 \quad (2\text{-}4)$$

C_{liquid} indicates the specific heat capacity of liquid water (4.2 J K^{-1} g^{-1}), T_0 (24.5 °C) is the initial temperature of the evaporator and T (35.5 °C) is the temperature of the evaporator surface. Δh_{100} represents the latent heat of vaporization of water at 100 °C and has a value of 2260 kJ kg^{-1}. Q_1 refers to the energy released by liquid water when it rises from temperature T to 100 ℃, Q_2 represents the energy released when water vapor drops from 100 ℃ to temperature T, and they can be obtained from equations 2-5 and 2-6:

$$Q_1 = C_{liquid} \times (100 - T) \quad (2\text{-}5)$$

$$Q_2 = C_{vapor} \times (T - 100) \quad (2\text{-}6)$$

In which, C_{vapor} is the specific heat capacity of water vapor is a constant of 1.865 J g^{-1} $°C^{-1}$.

In this work, the room temperature is 24.5 ℃ and the humidity in the environment is about 39.5%. According to the above formulas, the relevant calculations for the solar-driven water evaporation efficiency of **Fe_7Sn_6**-cellulose paper (10 mg cm^{-2}) are as follows:

$Q = 4.2 \times (35.5 - 24.5) = 46.20\ \text{kJ kg}^{-1}$

$\Delta h_{vap} = 4.2 \times (100 - T) + 2260 + 1.865 \times (T - 100) = 2410.61\ \text{kJ kg}^{-1}$

$h_{LV} = 46.20 + 2410.61 = 2456.81\ \text{kJ kg}^{-1}$

$\dot{m} = 0.71 - 0.198 = 0.512\ \text{kg m}^{-2}\ \text{h}^{-1}$

$C_{opt} = 1$

$P_0 = 1\ \text{kW m}^{-2}$

$\eta = 2456.81 \times 0.512 / 3600 = 34.94\%$

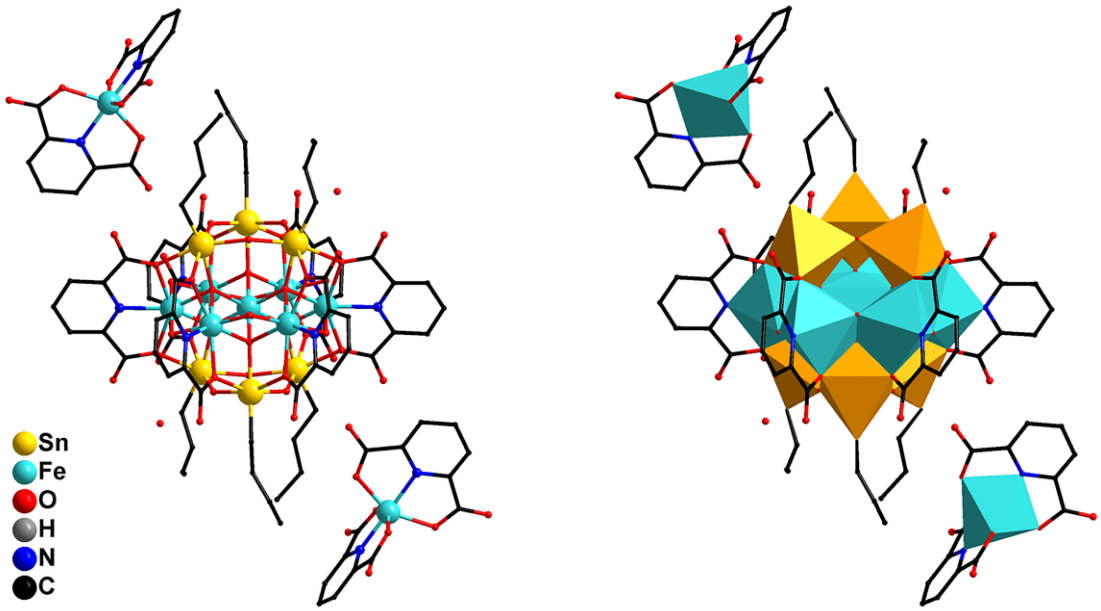

Figure S2. Ball-and-stick and polyhedral representations of **Fe_7Sn_6**. Polyhedral color code: light orange, SnO_5C; aqua, FeO_6N / FeO_4N_2.

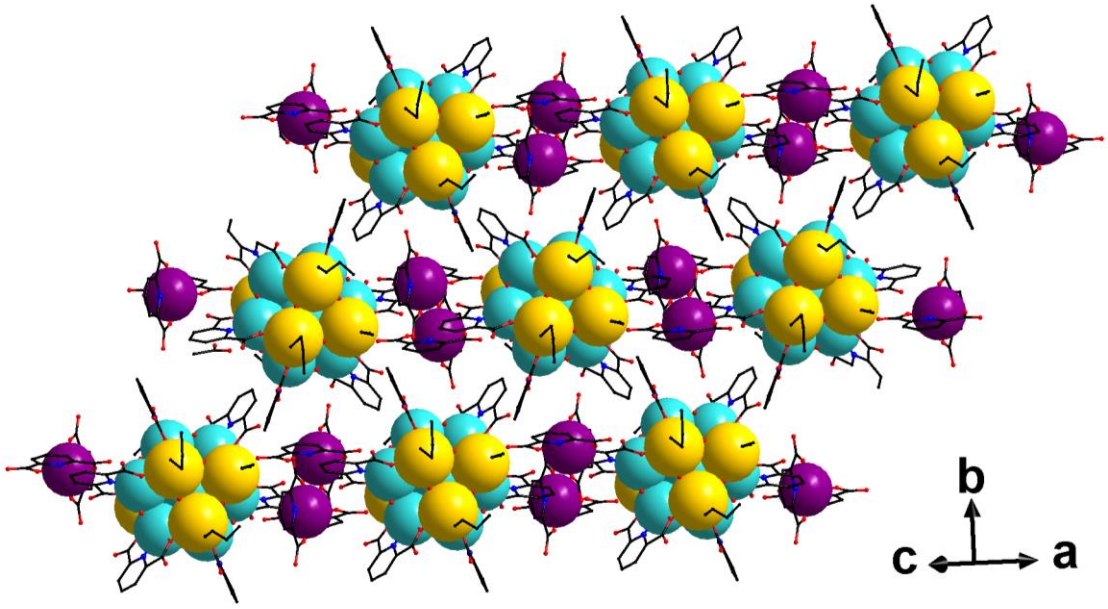

Figure S3. The packing view of **Fe_7Sn_6** along the direction of (1, 0, 1). Atom color code: Gold, Sn; aqua and violet: Fe; black: C; blue, N; red, O.

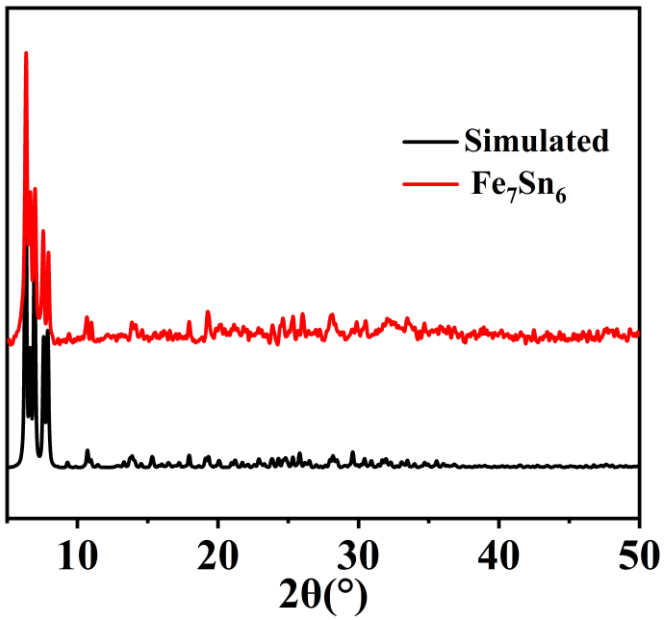

Figure S4. Simulated and experimental PXRD patterns of **Fe_7Sn_6**.

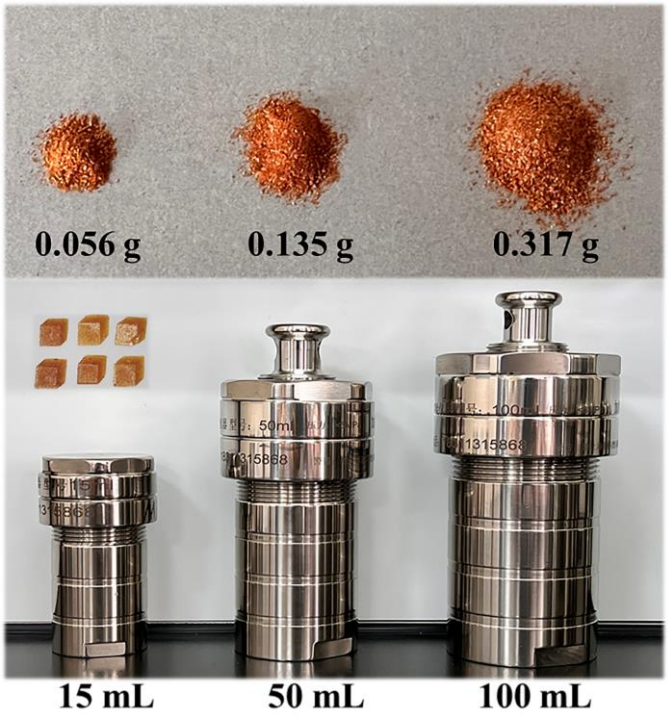

Figure S5. The scale-up synthesis of **Fe_7Sn_6**.

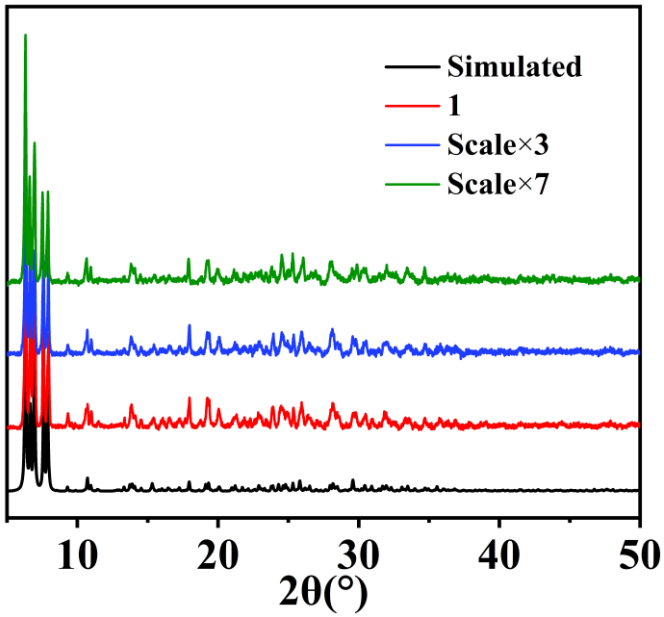

Figure S6. PXRD patterns of the simulated, experimental and scale-up synthesis of **Fe_7Sn_6**.

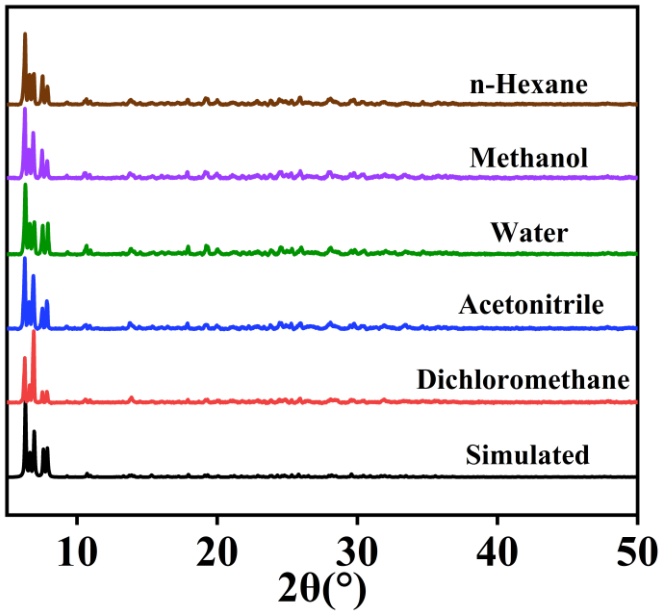

Figure S7. PXRD patterns of **Fe_7Sn_6** after soaking in common solvents for 36 h at room temperature.

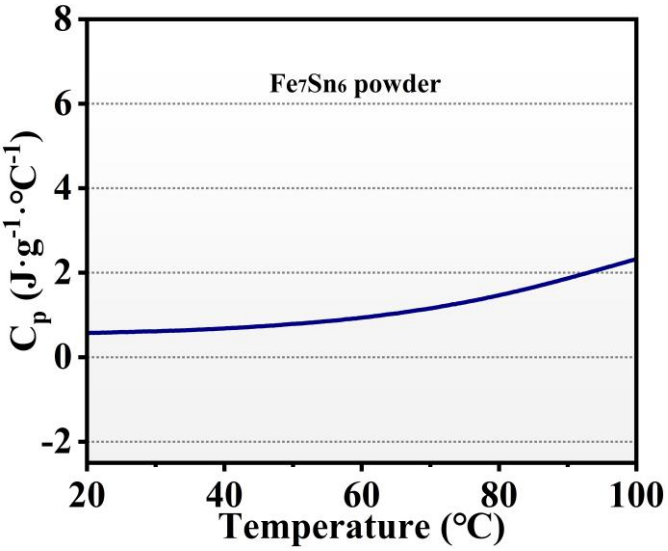

Figure S8. Specific heat capacity results of **Fe_7Sn_6** that obtained through DSC test. The averaged value of specific heat capacity at the range of 20–55 ℃ for the calculation of PTC efficiency is 0.682 J g^{-1} $℃^{-1}$.

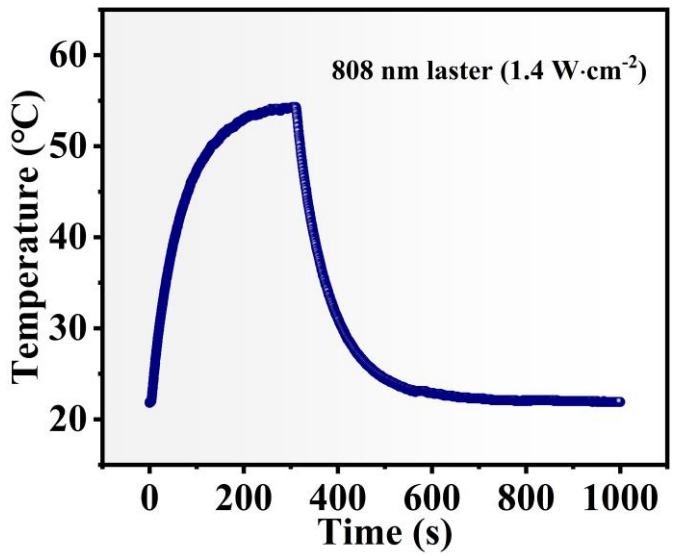

Figure S9. Heating–freezing curve of Fe_7Sn_6 excited by 808 nm-laser within 1000 s.

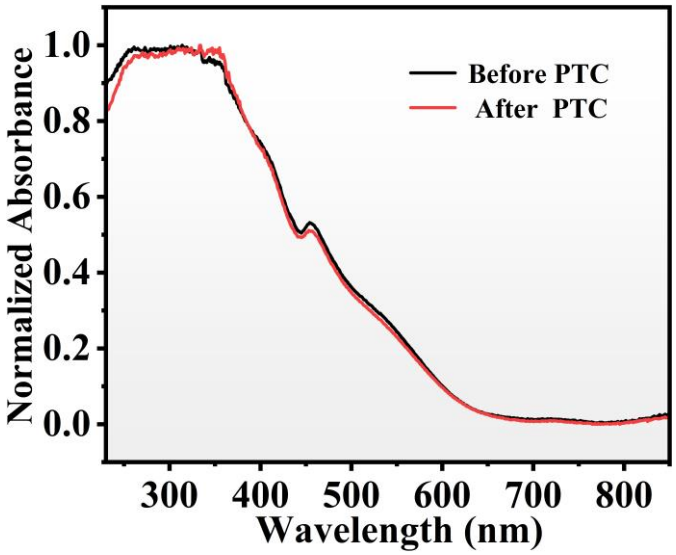

Figure S10. UV–vis absorption spectra of before and after photothermal conversion (PTC) of 13 mg Fe_7Sn_6 powder encapsulated in quartz slice.

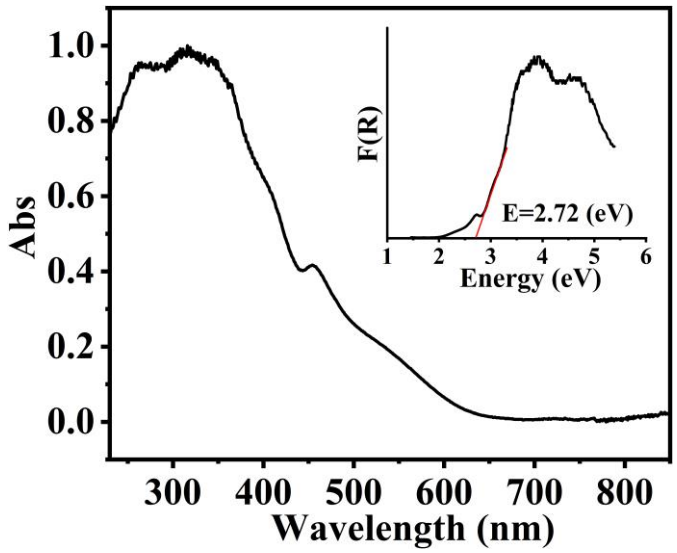

Figure S11. Solid-state UV−vis absorption and diffuse reflectance spectrum of **Fe_7Sn_6**.

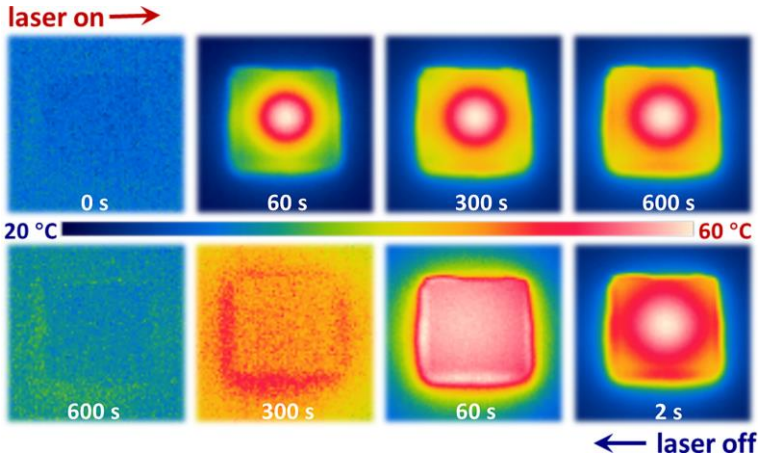

Figure S12. Thermal images of **Fe_7Sn_6** powder encapsulated in quartz slices during the 808 nm-laser (1.4 W cm^{-2}) on/off for 600 s.

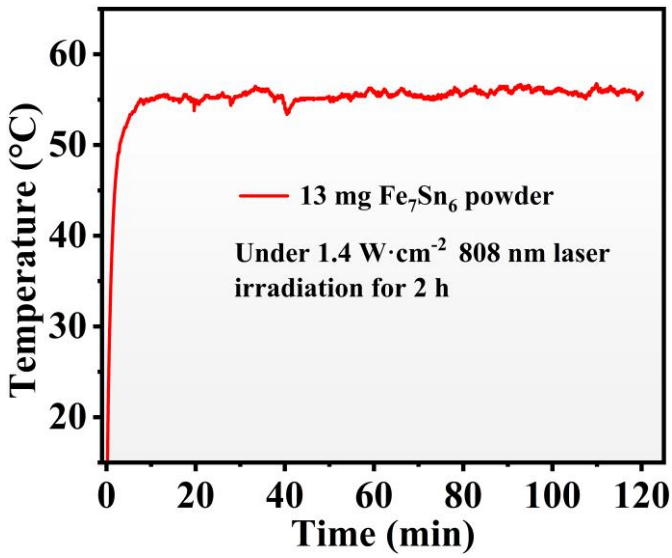

Figure S13. Time-temperature curve of 13 mg **Fe_7Sn_6** powder encapsulated in a quartz slice and irradiated continuously for 2 h under an 808 nm-laser at 1.4 W cm^{-2}.

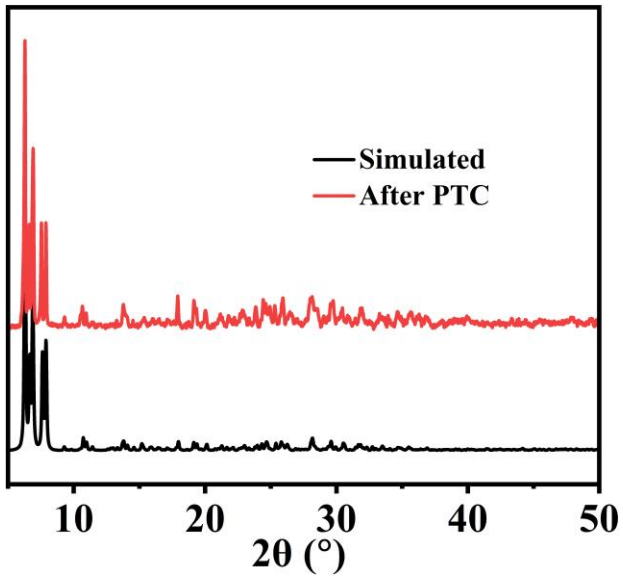

Figure S14. PXRD spectra of before and after photothermal conversion (PTC) of 13 mg **Fe_7Sn_6** powder encapsulated in quartz slice.

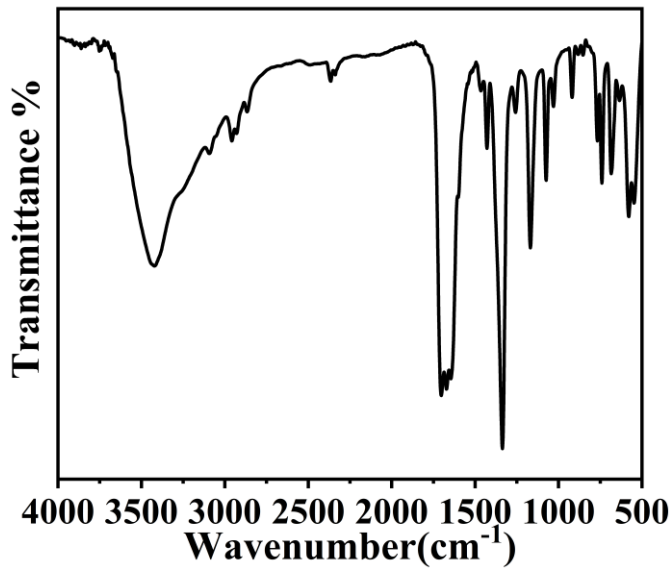

Figure S15. The FT-IR spectra of **Fe_7Sn_6**.

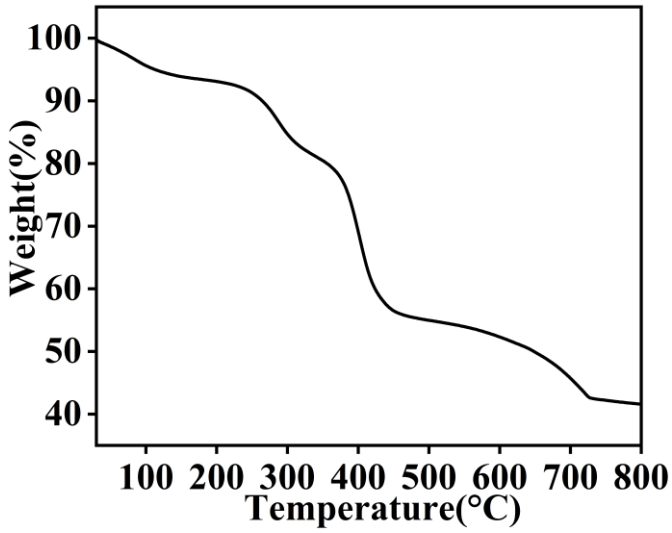

Figure S16. TG curve of **Fe_7Sn_6** in N_2 atmosphere.

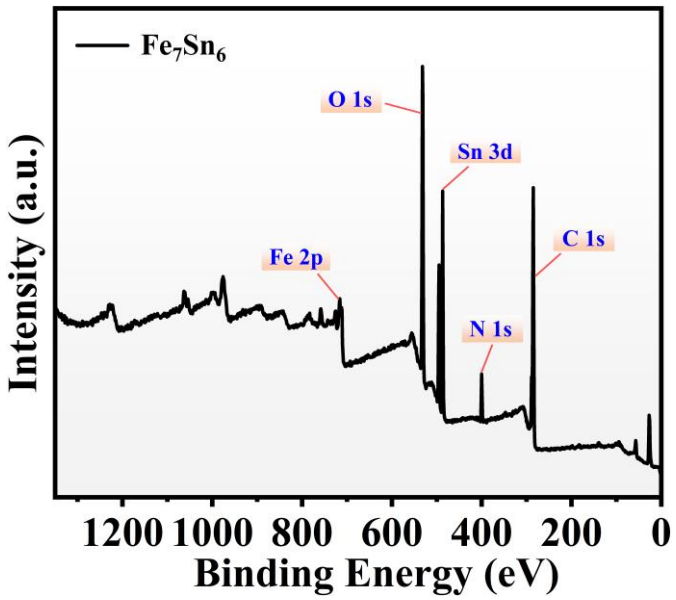

Figure S17. XPS survey spectrum of **Fe_7Sn_6**.

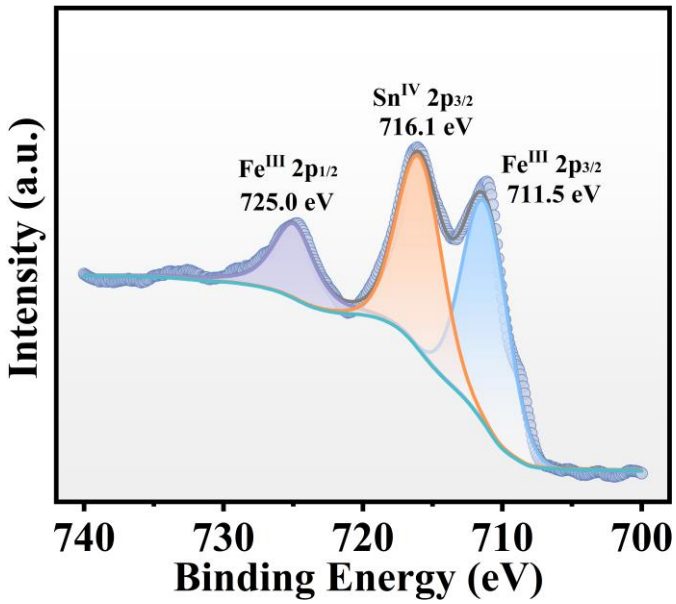

Figure S18. High resolution XPS spectra of Fe 2p and Sn 2p in **Fe_7Sn_6**.

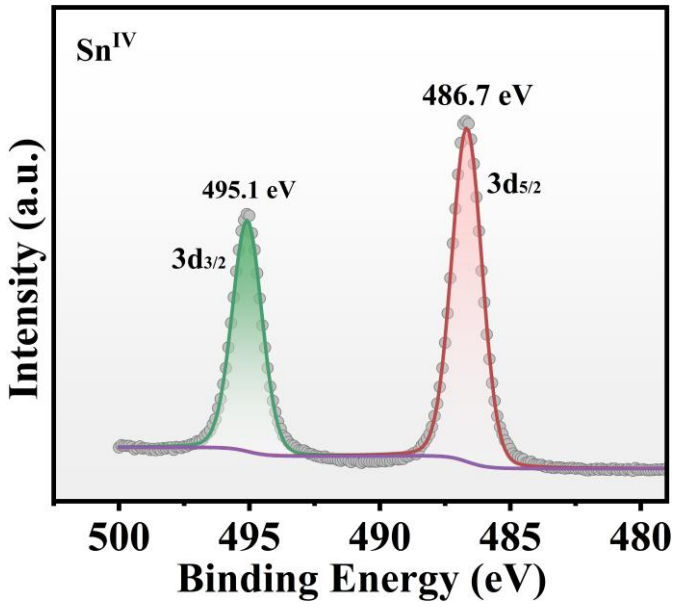

Figure S19. High resolution XPS spectra of Sn 3d in **Fe_7Sn_6**.

References

1. Sheldrick, G. M., *Acta Crystallogr. A* 2008, **64**, 112.
2. Sheldrick, G. M., *Acta Crystallogr. C*: *Struct. Chem.*, 2015, **71**, 3.
3. A. L. Spek, *Acta Crystallogr. C: Struct. Chem.,* 2015, **71**, 9.
4. Zhu, Y.; Olsen, M. R.; Nyman, M.; Zhang, L.; Zhang, J., *Inorg. Chem.* 2019, **58**, 4534.
5. Zhu, Y.; Zhang, J.; Zhang, L., *Inorg. Chem.* 2019, **58**, 15692.
6. Zhu, Y.; Zhang, L.; Zhang, J., *Chem. Sci.* 2019, **10**, 9125.
7. Zhu, Y.; Zhang, J.; Zhang, L., *Chem. Commun.* 2020, **56**, 1433.
8. Feng, C. C.; Zhang, Z.; Wang, Z. R.; Li, D. J.; Li, Q. H.; Zhang, L.; Zhang, J., *Inorg. Chem.* 2021, **60**, 1885.
9. Zhu, Y.; Li, D. S.; Zhang, J.; Zhang, L., *Inorg. Chem.* 2021, **60**, 1985.
10. Zhu, Y.; Li, D.; Zhang, J.; Zhang, L., *Chem. Commun.* 2022, **58**, 5650.
11. Liu, F.-F.; Wang, D.; Chen, G.-H.; Zhang, J.; Zhang, L., *J. Solid State Chem.* 2023, **321**, 123918.
12. Tian, X. J.; Yu, Y. Z.; Lu, Q.; Zhang, X. M., *Inorg. Chem.* 2022, **61**, 6037.
13. Lü, B., Chen, Y., Li, P., Wang, B., Müllen, K., Yin, M., *Nat. Commun.* 2019, **10**,

767.

14. Ke, H., Zhu, X.-M., Xie, S.-M., Ming, P.-X., Liao, J.-Z., *Inorg. Chem. Front.* 2022, **9**, 2568.
15. Zhang, M.-M., Chen, S.-L., Huang, S., Zheng, D., Liang, H., Ye, B., Chen, J., Song, X., Liu, L., Li, J., Chen, W., Ji, S., Dang, L., Li, M.-D., *J. Phys. Chem. Lett.* 2024, **15**, 68.
16. Chen, Y.-T., Wen, X.; He, J., Li, Z., Zhu, S., Chen, W., Yu, J., Guo, Y., Ni, S., Chen, S., Dang, L., Li, M.-D., *ACS Appl. Mater. Inter.* 2022, **14**, 28781.
17. Xu, J., Chen, Q., Li, S., Shen, J., Keoingthong, P., Zhang, L., Yin, Z., Cai, X., Chen, Z., Tan, W., *Angew. Chem. Int. Ed*. 2022, **134,** e202202571.
18. Ye, X., Chung, L.-H., Li, K., Zheng, S., Wong, Y.-L., Feng, Z., He, Y., Chu, D., Xu, Z., Yu, L., He, J., *Nat. Commun.* 2022, **13**, 6116.